Influence of positive active material type and grid alloy on corrosion layer structure and composition in the valve regulated lead/acid battery

R.J. Ball[a,*], R. Kurian[b], R. Evans[c], R. Stevens[a]

[a]*Department of Engineering and Applied Science, University of Bath, Bath, BA2 7AY, UK*
[b]*Hawker Ltd., Stephenson St. Newport NP9 0XJ, UK*
[c]*Invensys, Westinghouse site, Chippenham, Wiltshire, SN15 1SJ, UK*

Abstract

Performance of a valve regulated lead/acid battery is affected by the properties of the positive grid corrosion layer. An investigation has been carried out using a range of experimental techniques to study the influence of corrosion layer composition and structure on cyclic performance. A number of designs of battery were manufactured with different grids and positive active materials (PAMs). Two grid types were used consisting of either pure lead or a lead/tin alloy. Variations in PAM composition and structure were obtained by forming electrodes from grey oxide pastes containing additions of, red lead, tetrabasic lead sulphate, or sulphuric acid (sulphated). Results indicated that both grid alloy composition and PAM type affect the corrosion layer properties. Ultra-microtoming was used to prepare sections of the grid/corrosion layer interface. Results showed that corrosion propagated along tin rich grain boundaries.
© 2002 Elsevier Science B.V. All rights reserved.

Keywords: VRLA; Corrosion layer; EPMA; Ultra-microtoming

1. Introduction

The corrosion layer is one of the most important components of the positive electrode. Its properties will influence battery operation since electrons generated must flow through it. The ease with which electrons can flow is dependant on geometry, composition, structure and thickness. High currents can be generated as a result of the large difference in surface area between the positive active material (PAM) and grid. For a typical grid with a surface area of around 50 cm^2 the corresponding PAM area will be in the region of 500 m^2 [1].

The corrosion layer is first formed during plate curing and then increases in thickness as the battery is cycled. Thickness will be influenced by curing parameters such as temperature, humidity and oxygen concentration. Corrosion layers commonly consist of a multi-layered structure comprising of lead oxides of different stoichiometry. Normally the concentration of oxygen within the corrosion layer increases with distance from the grid. This is because oxygen must diffuse from the outer surface of the layer towards the grid.

The change in molar volume that occurs when Pb is oxidised to PbO$_2$ is >38%. A consequence of this is the generation of internal stresses, which cause cracks to form, when the corrosion layer reaches a critical thickness. This process occurs within the corrosion layer and at the corrosion layer/PAM interface. Non-uniform heating of the corrosion layer is another cause for the formation of cracks. Crack formation is undesirable as it reduces the strength and conductivity of the material. However, elastically compliant elements present within the corrosion layer and PAM offset this effect; these are commonly referred to as gel zones and allow stresses to be relieved and help in reducing the incidence of cracking [2,3]. The formation of gel zones is dependent on the state of hydration of the corrosion layer, which is influenced by the alloying elements present within the grid.

Lappe [4] investigated the relationship between electronic conductivity and stoichiometric coefficient of the lead oxides. He demonstrated that when the stoichiometric coefficient of an oxide reaches a value of 1.35 there is a rapid increase in conductivity and at 1.5, the conductivity is nearly equal to that of PbO$_2$. Lead oxides containing very small
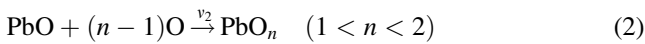
---

* Corresponding author. Tel.: +44-1225-386447;
fax: +44-1225-386098.
E-mail address: r.j.ball@bath.ac.uk (R.J. Ball).

amounts of oxygen exhibited conductivities around $10^{-10}\,\Omega^{-1}\,cm^{-1}$, whereas the conductivity of PbO_2 was $10^2\,\Omega^{-1}\,cm^{-2}$.

Growth of a corrosion layer is dependent on the initial oxidation of the grid to form lead monoxide. The lead monoxide must then react with more oxygen to form oxides of higher stoichiometric coefficient. These reactions have been expressed as chemical equations by Pavlov [1]. The three basic reactions that must occur in order to convert the lead grid into lead dioxide are reproduced as:

$$Pb + O \xrightarrow{v_1} PbO \tag{1}$$

$$PbO + (n-1)O \xrightarrow{v_2} PbO_n \quad (1 < n < 2) \tag{2}$$

$$PbO_n + (2-n)O \xrightarrow{v_3} PbO_2 \tag{3}$$

The rate of each of the reactions above can be described in terms of a rate coefficient. Depending on the relative rates of the reactions, corrosion layers having different stoichiometric coefficients will be formed. By considering the stoichiometric coefficient and conductivity, Pavlov [1] proposed the following general rules:

$v_1 > v_2$	Low valency lead oxide	High specific resistivity corrosion layer
$v_1 < v_2, v_3$	High valency lead oxide	Low specific resistivity corrosion layer

In addition to these reactions, the self-discharge reaction between Pb and PbO_2 should also be considered. This rate is determined by a fourth rate coefficient v_4.

$$Pb + PbO_2 \xrightarrow{v_4} 2PbO \tag{4}$$

The occurrence of this reaction leads to a decrease in the overall stoichiometric coefficient of the oxide and to an increase in specific resistivity of the corrosion layer.

The alloying elements present in the grid alloy influence the structure of the corrosion layer by determining the type and rate of reactions occurring [5]. A consequence of this is a variation in stoichiometric coefficient of the oxides and therefore conductivity of the corrosion layer.

Work conducted by Pavlov [1] and colleagues indicated that alloying additions within the grid influence the conductivity of the corrosion layer by either acting as an electro catalyst or as an inhibitor to the reactions given by Eqs. (1)–(4) [6,7]. Tin catalyses reactions 2 and 3, and as a consequence corrosion layers with higher stoichiometric coefficients are observed.

Passivation of the positive plate is associated with the formation of lead monoxide. If the thickness of this layer exceeds a critical value, it acts as a high resistance strata within the corrosion layer which can insulate the grid from the active material. The overall effect is to decrease the voltage at which discharge will occur on the plate. Passivation occurs via the reaction, $Pb + O \rightarrow PbO$, where

the electrode system $Pb/PbO/PbO_2$ is formed. At open circuit the self-discharge reaction, $Pb + PbO_2 \rightarrow 2PbO$ occurs, also producing the high resistance lead monoxide layer [8]. The rate at which passivation occurs on the positive plates can be affected by dopants such as tin present within the grid alloy and corrosion layer. Tin has the effect of increasing the conductivity of the PbO layer [7,9].

Depassivation can occur by two processes, the first being the reduction of PbO to Pb by cathodic valency [9] and the second by oxidation of PbO by the oxygen generated during overcharge, which produces a lower resistance oxide with higher valency [1].

2. Production of test batteries

The batteries examined in this study were all 40 amp h valve regulated lead/acid batteries. Hundred percent glass separator paper and a standard cyclic negative active material were used in all batteries however, variations were made to the PAM and grid alloy. Two different grid and three types of PAM were used in total. A summary of the different battery types, which were constructed referred to as A–E, is given in Table 1.

The grey oxide (cyclic) PAM used in the manufacture of the type A battery was formed from a positive paste mix consisting of 90% grey oxide (α-PbO, $\approx$29% lead), 10% red lead, sulphuric acid and distilled water. Battery types B and C consisted of PAM formed from a grey oxide & tetrabasic lead sulphate positive paste produced from a mixture of grey oxide, tetrabasic lead sulphate, sulphuric acid and distilled water. A sulphated grey oxide paste was used in the production of positive electrodes for battery types D and E. This consisted of grey oxide, extra sulphuric acid compared to the other pastes and distilled water.

The battery grid production route can be described in two stages, the first of these being production of lead strip of suitable thickness, and the second, punching of the strip to form the grid. Two different grid types were used in the construction of the test batteries. The initial stage in grid production involves the manufacture of a lead strip. Hence, lead grid was manufactured firstly by casting pure lead into a strip several centimeters thick. The lead strip was then rolled repeatedly until the desired thickness was obtained. Lead/tin grids were manufactured using Comminco casting

Table 1
PAM and grid types used in the test batteries

Battery type	PAM	Positive grid
A	Grey oxide (cyclic)	Pure lead
B	Grey oxide and tetrabasic lead sulphate	Pure lead
C	Grey oxide and tetrabasic lead sulphate	Lead/tin
D	Sulphated grey oxide	Pure lead
E	Sulphated grey oxide	Lead/tin

machines. This process has the ability to cast the grid to the required thickness without the need for subsequent rolling. Once the lead strip was obtained, holes for the active material, having dimensions 4 mm × 13 mm were introduced using a punching machine, converting the strip into a grid. Pressing the paste into the lead current collecting grid produced battery electrodes. A glass paper was applied to each side of the paste impregnated lead grid, to ease handling, prior to the cutting our of individual electrodes. Electrodes were subjected to a curing stage before cell assembly. Compositional analysis of cured electrodes using X-ray diffraction and wet chemical analysis indicated that groups A, D and E consisted almost entirely of α-lead monoxide except for a small amount, ∼5%, of unreacted metallic lead. Groups B and C contained approximately 30% tetrabasic lead sulphate and 4% metallic lead, the remainder consisting of α-lead monoxide. After battery assembly the positive plates were converted to lead dioxide during the formation stage of manufacture. X-ray diffraction analysis of the PAM indicated an α:β lead dioxide ratio of approximately $50\% \pm 10\%$, with a small proportion, 10%, lead sulphate present in some plates.

3. Cycling of test batteries

Cycling was carried out automatically using Digitron charging units. Each cycle consisted of a constant current discharge at 7.05 A to 10.2 V followed by a constant voltage recharge at 14.7 V for 16 h. This was repeated until the capacity after charging was <80% of the initial starting capacity. The cells that showed the greatest and least reduction in voltage during a final discharge/charge cycle were examined; these are referred to as the 'bad' and 'good' cells respectively. An example of the voltage in each of the six cells of a battery during the last discharge charge cycle is shown in Fig. 1.

4. Sample preparation

4.1. Materialography

Cross-sections of the corrosion layers from each of the battery types examined in this study were prepared using standard techniques. After initial encapsulation in resin battery electrodes were sectioned and remounted for polishing. Silicon carbide paper was used to grind and flatten the samples, followed by polishing with an alumina suspension and finally by vibratory polishing. A more detailed description of the preparation method is given in an earlier paper [10].

4.2. Grid/corrosion layer interfacial analysis

Although mechanical polishing of cross-sections was successful for obtaining images of corrosion layers several tens of microns thick, using this method it proved impossible to obtain an image of sufficient quality of the grid/corrosion layer interface. This was attributed to the difference in properties between the soft lead grid bar and the hard lead oxide ceramic corrosion layer, which wore down at different rates under the same polishing media. Ultra-microtoming, however, when used was a successful method of sample preparation.

Ultra-microtoming, although employed mainly for biological samples, can be used for the preparation of metals and ceramics. For the purpose of obtaining a good quality grid/corrosion layer cross-sectional sample, the microtome needs only to be used as a tool to obtain a flat surface that can then be examined by scanning electron microscopy.

Samples were produced by cutting sections of grid bar out of a positive electrode and then breaking away the PAM. Due to the relative strengths of the grid/corrosion layer bond and corrosion layer/active material bond, the corrosion layer stayed attached to the grid in the majority of instances.
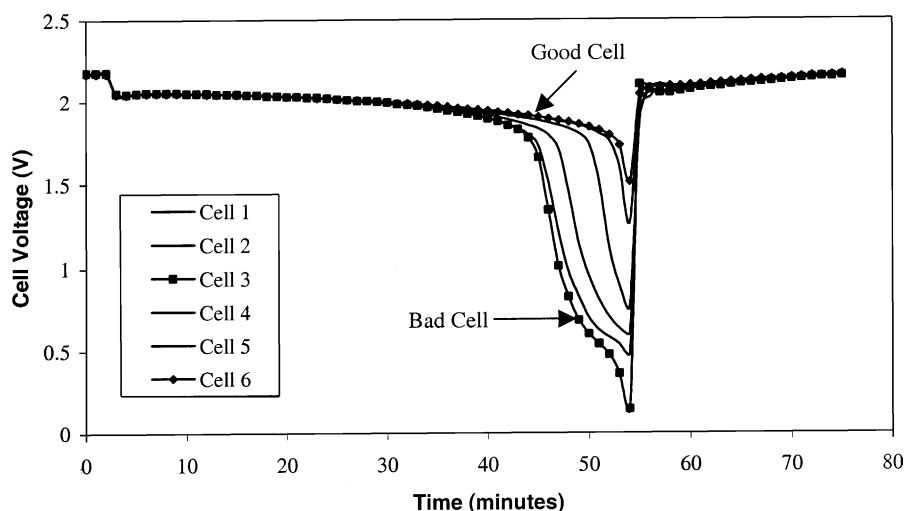

Fig. 1. Plot of voltage vs. time for cells in battery type C.

Table 2
Standards used for electron probe microanalysis

Element	Possible 'states' of element in sample	Standard selected and source	Notes
Lead, Pb	Pb, PbO_n ($1 < n < 2$)	Lead monoxide, PbO	Lead is present in the form of lead or lead oxide, this standard gives a good match in composition and structure
Oxygen, O	PbO_n ($1 < n < 2$)	Lead monoxide, PbO	The standard is almost identical in composition to the sample, therefore this is a very good match
Tin, Sn	Sn, SnO_n ($1 < n < 2$)	Pure tin, Sn (C.M. Taylor Corp., 12921-5)	This is again a suitable standard to use
Sulphur, S	R-SO_4	Iron Sulphide (pyrite), FeS_2 (C.M. Taylor Corp., 11540-1)	The sulphate and sulphide are likely to have varying characteristics Errors may therefore be slightly larger than with the previous elements

Once a section of grid bar was obtained with a uniform layer of corrosion and a minimum amount of PAM attached, it was cast in resin using specially designed latex moulds for the ultra-microtome. Soaking for 4 h prior to curing ensured a good resin to sample contact. Curing was achieved by heating in an oven at 60 °C for a period of at least 24 h.

Once cured, the sample was trimmed to a suitable size and dimensions for ultra-microtoming. Initially sections were removed from the surface using a glass knife prior to removal of sections using a diamond knife in order to obtain as clean a cut as possible for examination. A thin layer of gold was deposited onto the surface of the finished section to prevent charging of the resin in the SEM. This was done using an Edwards sputter coating unit.

5. Experimental methods

5.1. Microscopy and corrosion layer thickness measurement

The polished cross-sections of corrosion layers from each battery type were examined and photographed using a Zeiss ICM405 optical microscope. Microtomed sections were examined in a Jeol 6310 scanning electron microscope. Corrosion layer thickness measurements were determined using Optimas image analysis software [11]. Images were obtained using a digital camera and then measurements taken on the top, bottom, left and right hand sides of five grid bars from each battery, thus producing 20 readings in total. The mean of these readings was then quoted as the corrosion layer thickness.

5.2. Electron probe microanalysis

A Jeol JXA-8600 superprobe was used to determine the composition of the corrosion layers in each of the samples tested. Readings were taken in a line across the corrosion layer thickness at 1 μm intervals. An initial qualitative analysis indicated that the corrosion layer consisted of lead, oxygen, sulphur and tin. Details of the expected oxidation states of these elements and the standards used are given in Table 2.

To prevent charging effects the samples were coated with a thin layer of carbon, using an Edwards sputter coating unit. All samples and standards were coated simultaneously to reduce errors caused by adsorption of X-rays by the layer. Taking into account the peak size, shape and position, the diffraction crystals employed and counting times used are shown in Table 3.

6. Results

6.1. Optical examination of corrosion layer

Examination using an optical microscope of the corrosion layers for each battery type indicated variations in structure and morphology. A typical corrosion layer, from a type A battery is shown in Fig. 2. The lead grid is out of focus in the photograph, however this is an unavoidable consequence of the preparation method used. Cracking can be seen parallel to the grid surface running along the 'grid side' of the corrosion layer. No porosity is visible within the corrosion layer and an internal boundary within the corrosion layer is visible in the central region.

Table 3
EPMA settings for quantitative analysis

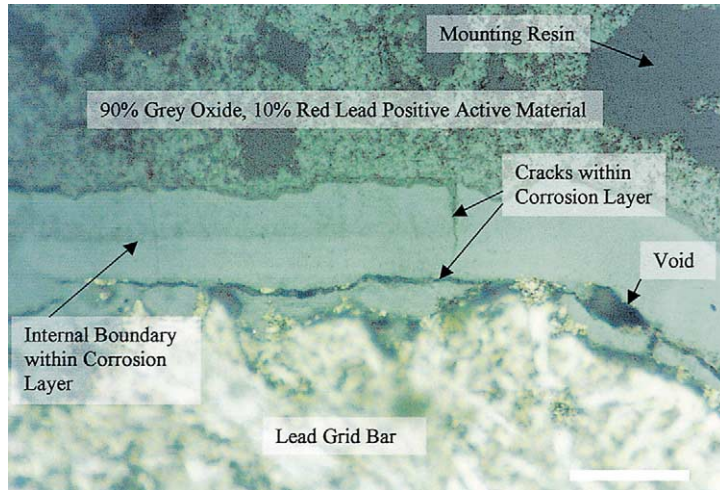| Element	Line	X-tal	Peak position (mm)	Peak background (mm)		Counting time (s)	
				Lower	Upper	Peak	Background
Lead, Pb	$M\alpha_1$	PET[a]	169.090	4.000	4.000	30.0	5.0
Oxygen, O	$K\alpha_1$	LDE[b]	109.440	8.800	8.800	30.0	5.0
Tin, Sn	$L\alpha_1$	PET[a]	115.125	4.000	4.000	10.0	5.0
Sulphur, S	$K\alpha_1$	PET[a]	172.010	0.800	0.800	10.0	5.0

[a] Pentaerythritol.
[b] Tungsten/silicon multilayer.

Fig. 2. Corrosion layer from type A battery (scale bar 50 microns).
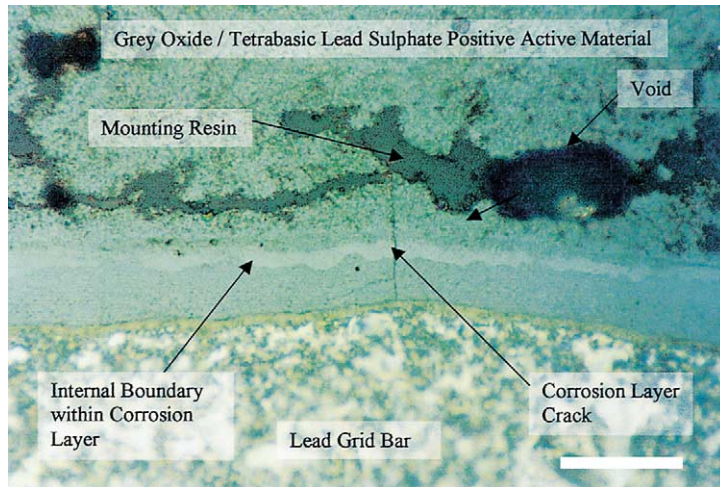
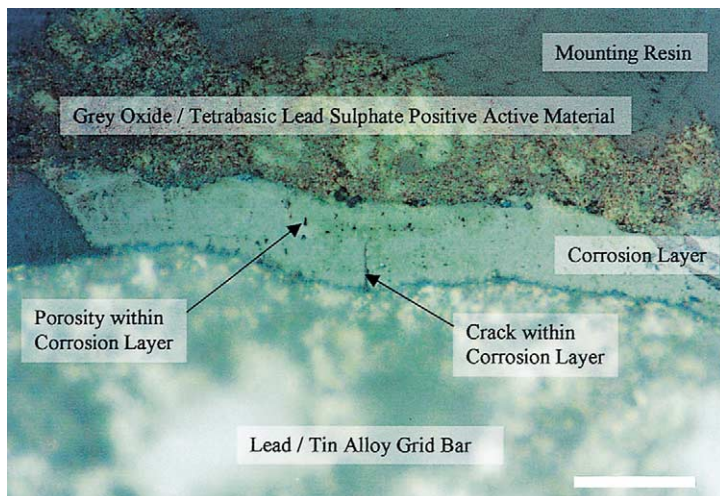Fig. 3. Corrosion layer from type B battery (scale bar 50 microns).

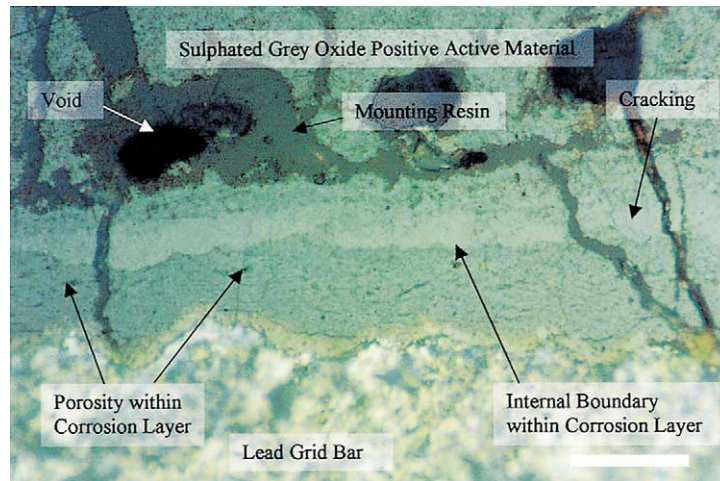Fig. 4. Corrosion layer from type C battery (scale bar 50 microns).

Fig. 5. Corrosion layer from type D battery (scale bar 50 microns).
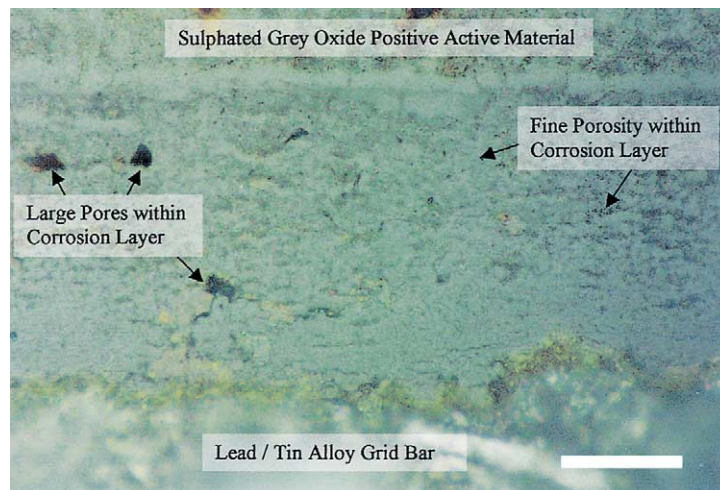

Fig. 6. Corrosion layer from type E battery (scale bar 50 microns).

The corrosion layer observed on the type B battery grid, Fig. 3, is very similar in appearance to the previous one except that the internal boundary within the layer is closer to the PAM and lighter in colour. Fig. 4 shows the corrosion layer from the type C battery. No internal boundary is identifiable in this layer and a number of black spots are visible which are believed to be pores.

The type D positive electrode has a greater volume fraction of porosity, consisting of large numbers of cracks in the corrosion layer and PAM (Fig. 5). Large pores are also visible in the PAM adjacent to the corrosion layer. Fig. 6 shows a typical corrosion layer from a type E battery. Fine porosity is visible across the width of the layer and a number of larger pores are also present. A lighter band in the corrosion layer is visible adjacent to the PAM.

Corrosion layer thickness measurements taken on the good and bad cells of the batteries examined and the number of cycles at which these values were taken are shown in Table 4. There is no significant difference between the corrosion layer thickness measurements for the good and

bad cells. The thickest layers occurred on batteries of type D and E (ignoring type B due to higher cycles). These layers contained more pores and therefore would have allowed oxygen gas to readily diffuse to the grid/corrosion layer interface. When a comparison is made between type D and E batteries, type E that contained the lead/tin grid has a thicker layer. This suggests that tin promotes an increase in corrosion layer thickness. However, the same conclusion cannot

Table 4
Oxide thickness measurements

Battery type	Cycles	Good cell (μm)		Bad cell (μm)	
		Average	S.D.	Average	S.D.
A[a]	28 and 42	23.5	6.6	19.8	3.1
B	40	47.7	12.7	40.0	11.0
C	29	28.1	5.3	25.5	5.8
D	29	47.5	8.8	50.8	5.9
E	27	89.4	12.6	88.1	14.4

[a] Data averaged for batteries cycled 28 and 42 times.

be drawn from the batteries from type B and C, since the type B battery sustained significantly more cycles. The thinnest corrosion layer occurred on the positive grid of battery type A.

6.2. Structural and compositional analysis of corrosion layer using EPMA

A compositional analysis of the corrosion layer was carried out using electron probe microanalysis. This involved obtaining electron images of the corrosion layers, which proved useful in providing additional information on layer porosity.

The main results of interest are quantitative, however, the qualitative results will be considered first. Lead, oxygen and sulphur were identified in all corrosion layers with the addition of tin in the case of those attached to a grid bar originally alloyed with tin. This indicates that tin contained initially within the grid becomes incorporated into the corrosion layer during growth. The fact that no other elements were identified, with the exception of carbon, which was used as a conductive coating, demonstrates that the materials used to manufacture the battery were pure and did not contain detectable amounts of any other element.
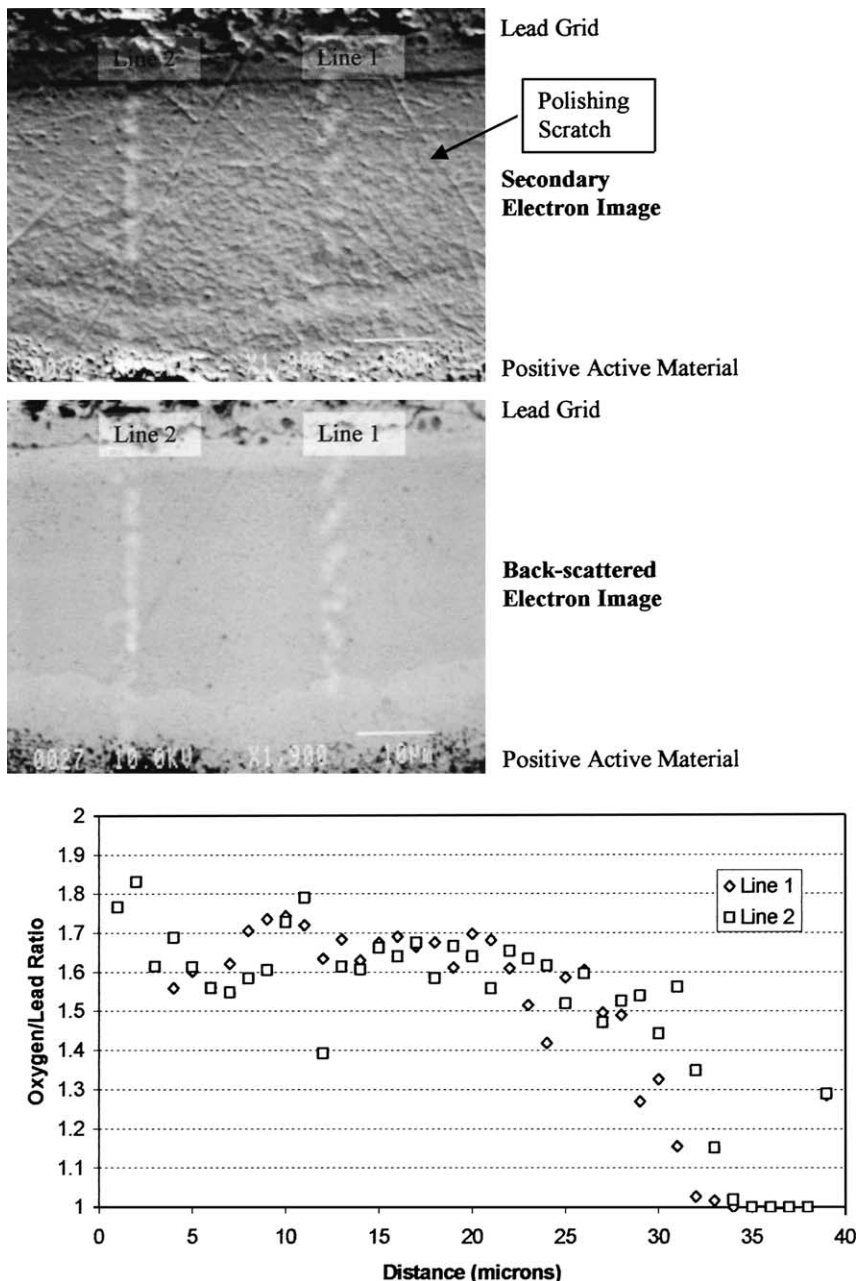

Fig. 7. Analysis of corrosion layer from battery type A.

Initial spot quantitative analyses on the corrosion layers examined, showed a large variation in compositional values, obtained due to the presence of porosity and surface roughness. The surface roughness is clearly visible in the scanning electron images and porosity in the back-scattered electron images, Figs. 7–11. This can be explained by considering the interactions of the incident electrons with the sample and the method used to calculate the quantity of each element present.

Calibration of the electron probe microanalyser was achieved with the use of known standards. However, with this approach the accuracy of the analysis is dependent on the unknown sample and standards having similar densities. Porosity within the corrosion layers can effectively reduce their physical density and introduces errors into the results.

When X-rays from the sample are counted the analysis software automatically assumes that the sample is 100% dense, if a pore is present, the number of X-rays emitted is reduced and the calculation of the composition altered. This is demonstrated by the typical analysis given in Table 5.

The accuracy of an elemental analysis can be determined by considering the total weight percent; the closer it is to 100%, the more accurate the analysis. For the purposes of
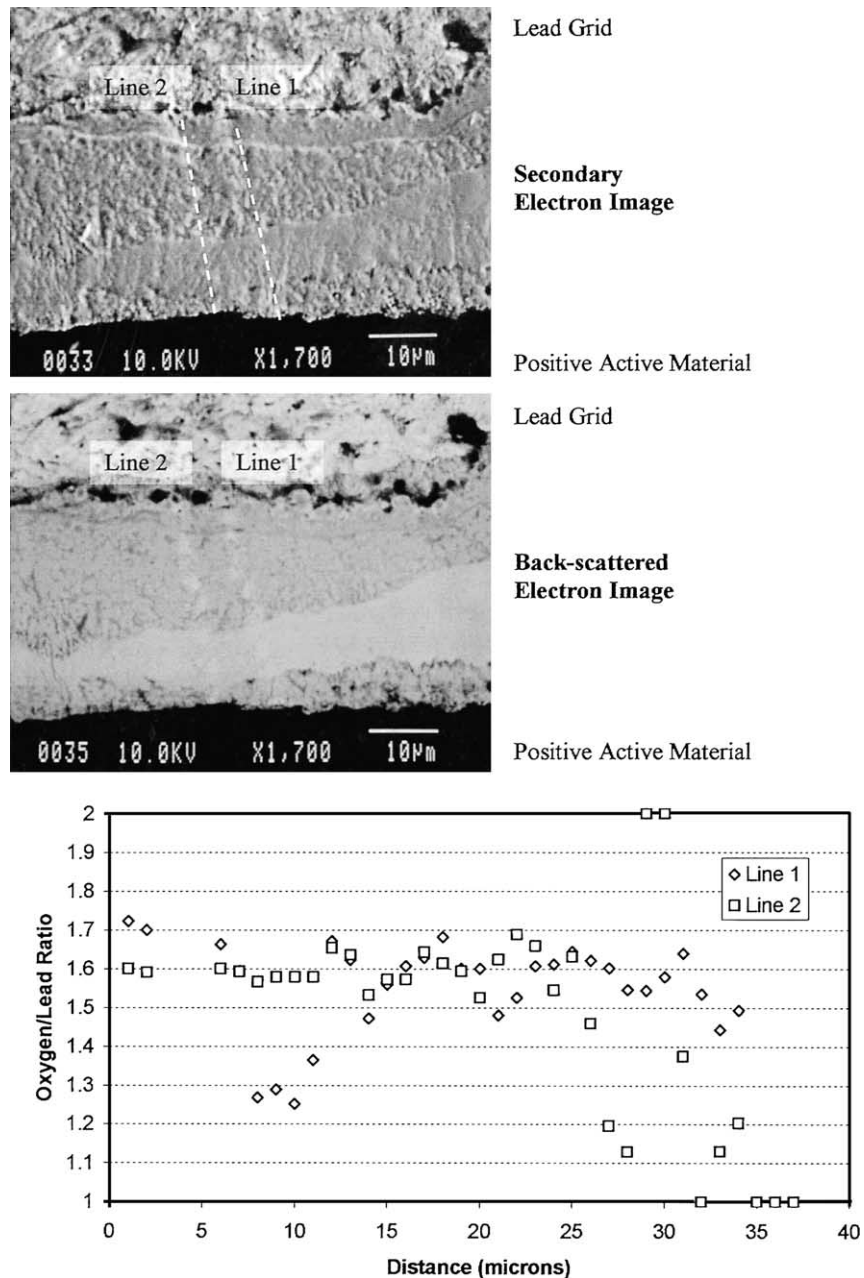

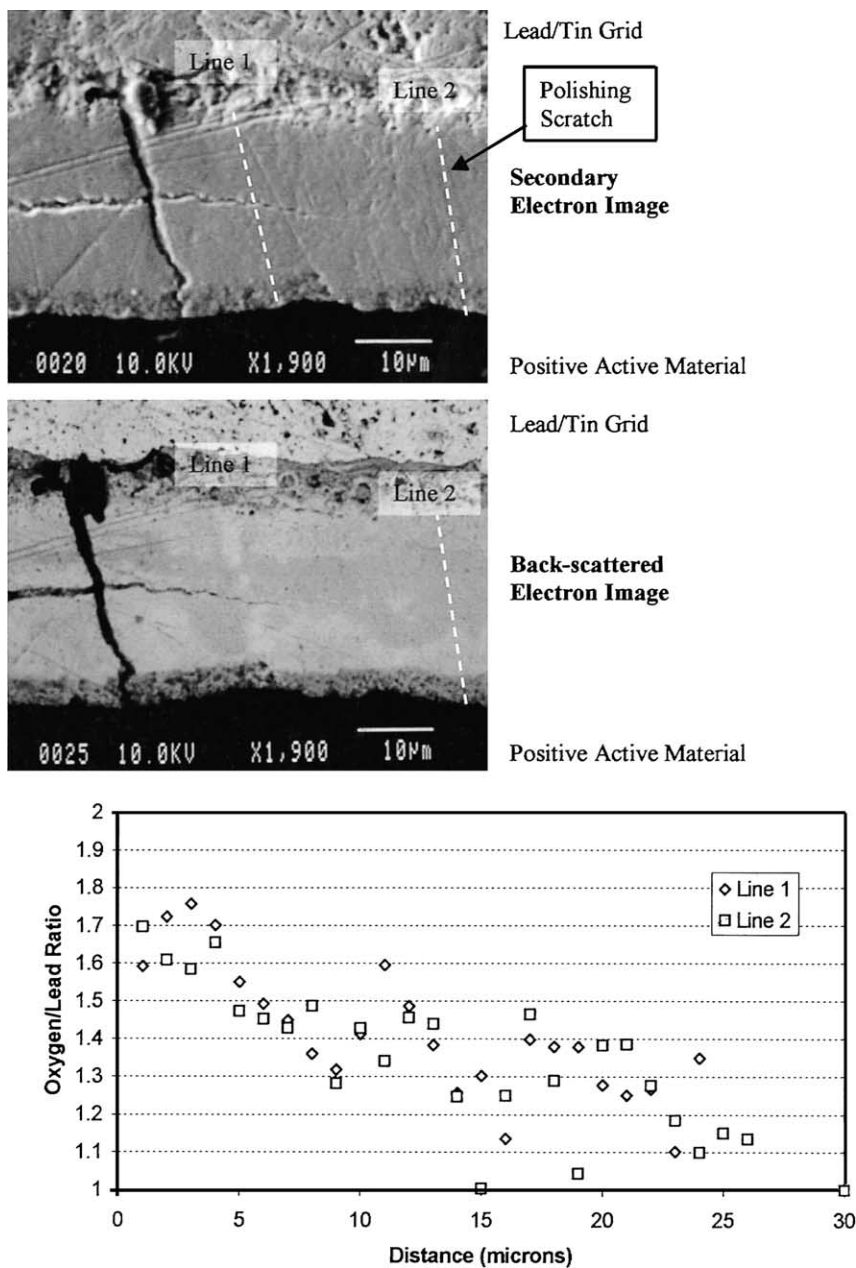Fig. 8. Analysis of corrosion layer from battery type B.

Fig. 9. Analysis of corrosion layer from battery type C.

this study all the analyses with a combined weight percent of <90% were ignored as it was considered this indicated that the region of sample excited by the electron beam contained an unacceptable level of porosity or surface roughness.

Table 5
Typical EPMA compositional analysis

Atom	Percentage
Pb	43.4
O	56
S	0.6
Sn	0.1
Total wt.%	96.1

In order to obtain an accurate value for the oxide stoichiometry, a large number of quantitative analyses were conducted. As variations in oxide stoichiometry between the inner and outer edges of the corrosion layer are of interest, a quantitative line scan between these two positions was the most appropriate option.

Analyses were conducted at 1 μm intervals along the scan line. This provided the maximum number of practical analysis points considering that the minimum area that can be analyzed is approximately 1 μm in diameter. The maximum number of analysis points was used, since for the more porous samples a large number of the analyses were rejected because the total weight percent was <90%. To calculate the stoichiometry of the oxide in the corrosion
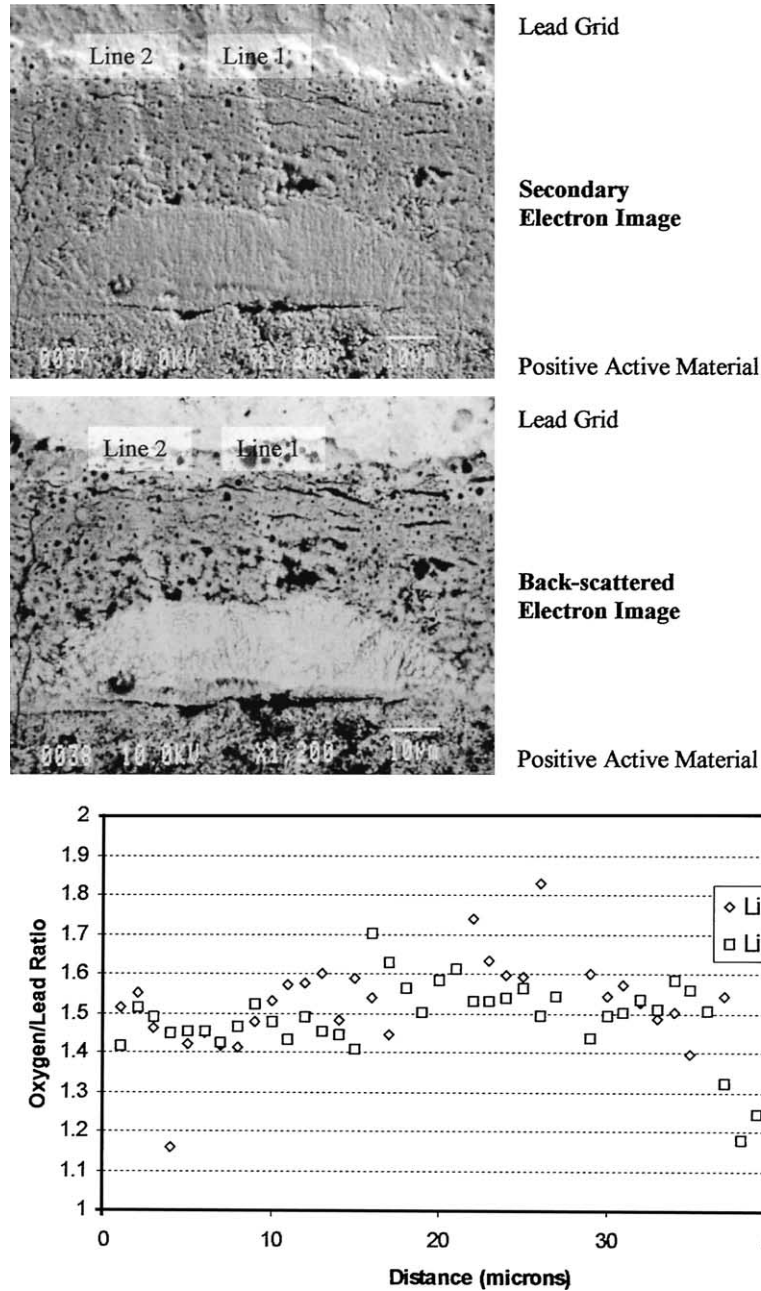
Fig. 10. Analysis of corrosion layer from battery type D.

layer it is necessary to make a number of assumptions for each analysis. These are summarised as follows:

- The only elements present in the corrosion layer are lead, oxygen, tin and sulphur.
- All sulphur present within the corrosion layer is in the form of a metal sulphate.
- Lead and tin within the corrosion layer are either in the form of an oxide or sulphate.
- Oxide stoichiometry for a given analysis point is always the same regardless of metal e.g. lead or tin.

From these assumptions a number of expressions, shown later, were derived to obtain values for the total metal and oxygen atoms available for incorporation into oxide, thus allowing the stoichiometry of the oxide to be calculated.

Total metal atoms forming oxide, $\quad T_M = P + T - S$ (5)

Total oxygen atoms forming oxide, $\quad T_O = O - (4 \times S)$ (6)

Oxide stoichiometry ratio, MO_n, $\quad n = \dfrac{T_O}{T_M}$ (7)

Where P is the number of lead atoms identified in analysis, T the number of tin atoms identified in analysis, S the number
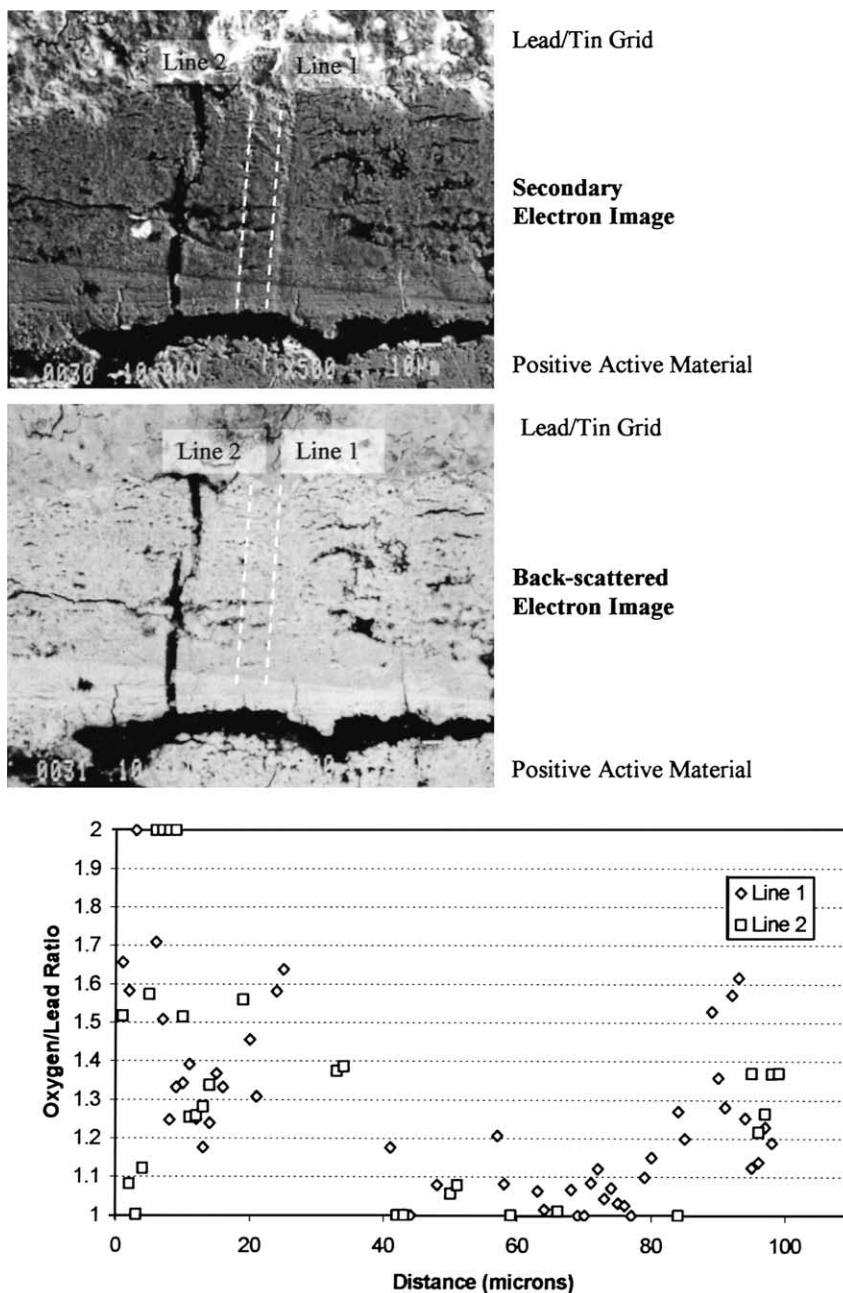
Fig. 11. Analysis of corrosion layer from battery type E.

of sulphur atoms identified in analysis and O the number of oxygen atoms identified in analysis.

Secondary and back-scattered electron images and plots of oxygen/lead ratio versus distance across corrosion layer for each of the battery types examined are shown in Figs. 7–11.

The electron scanning process resulted in a layer of contamination being deposited on the corrosion layer surface. This provided a means to identify the exact position of the scan line. For all plots the scan direction taken was from the active material towards the grid bar. Variations in oxygen/lead ratio occur with distance across the corrosion layer and also between the different battery designs. There is a general trend showing a decrease in oxygen content towards the grid bar. When comparing the scan lines and plots, step variations in oxygen/lead ratio do not always correspond to the spatial position of internal boundaries within the corrosion layer.

Scatter in some of the data plots is believed to be caused by errors introduced by variations in surface roughness and porosity. Despite these factors it has still proved possible to identify general compositional trends within the corrosion layer of each battery design.

Internal boundaries within the corrosion layers can be identified in both back-scattered and secondary electron
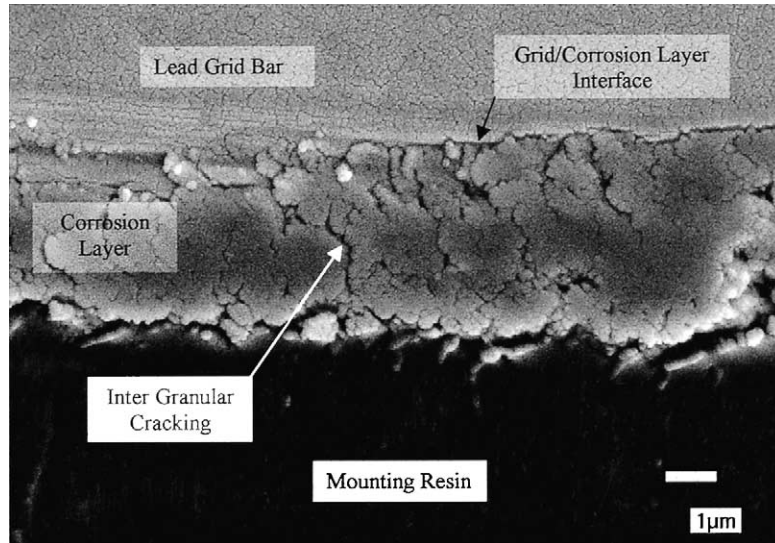
Fig. 12. Grid corrosion layer interface from type B battery.

images by darker and lighter regions of contrast. The darker regions correspond to lower atomic mass areas and the light regions to high. Variations in intensity and contrast are a consequence of the back-scattered electron intensity dependence on atomic number. This can be used to explain the light shade of the grid bar, which has a high average atomic mass and is therefore efficient at back-scattering electrons.

From an examination of the images it can be seen that the lighter band within the corrosion layer is positioned adjacent to the PAM and the darker band to the grid bar. This observation suggests an increased lead content in the corrosion layer adjacent to the PAM. This cannot be explained when it is presumed that the oxygen concentration is considered to be higher in these regions, suggesting the materials may have different work functions, thereby producing a variation in contrast between the different regions.

6.3. Analysis of the corrosion layer/grid interface

Preparation of corrosion layers using grinding and polishing techniques produced a high quality surface finish suitable for electron microscopy and, wave and energy dispersive analysis. However, the differences of material removal rate between the soft lead grid and hard ceramic corrosion layer make examination of this interface almost impossible due to the ledge formed at the interface. For this reason, the alternative technique of ultra-microtoming was used. This not only provided a flat section, but the disruption to the interface was negligible making detailed microscopy feasible.

Samples were prepared from the freshly formed positive electrodes of battery types B–E. Secondary electron images of the sections taken are shown in Figs. 12–15, respectively. From the figures it can be seen that this technique provides
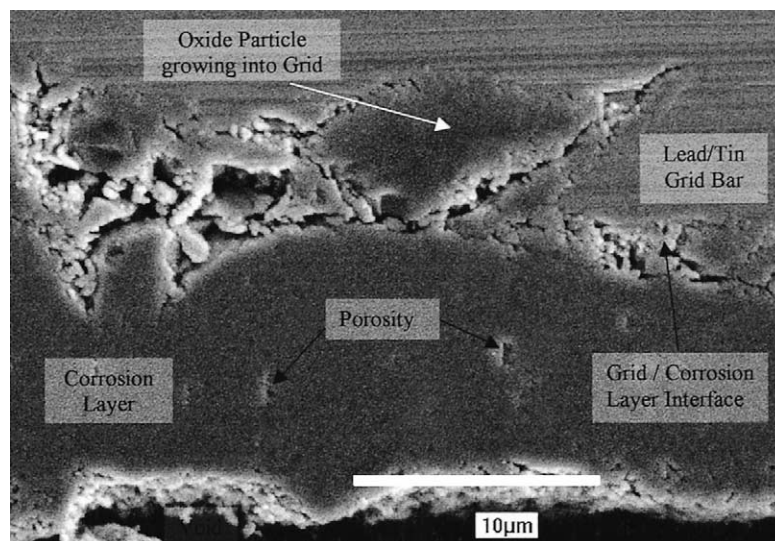

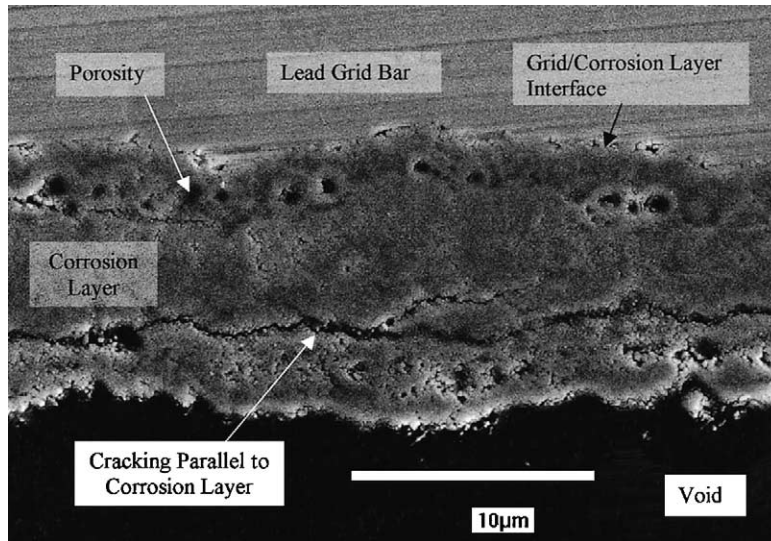Fig. 13. Grid corrosion layer interface from type C battery.

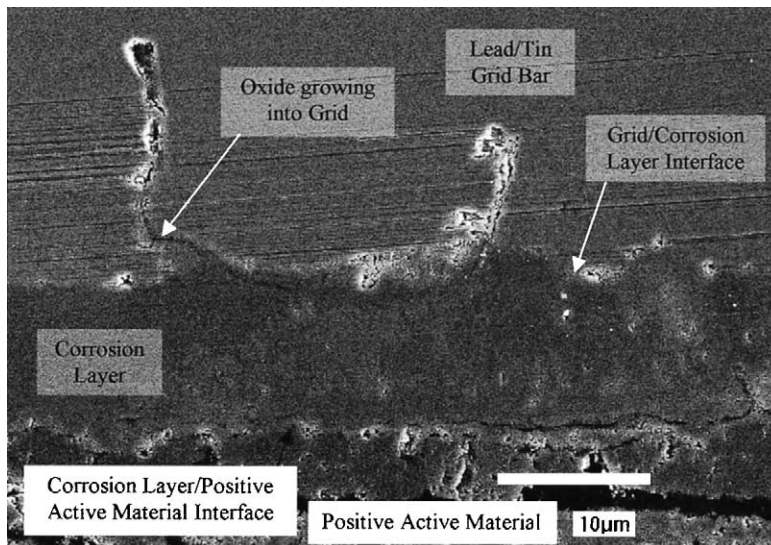Fig. 14. Grid corrosion layer interface from type D battery.

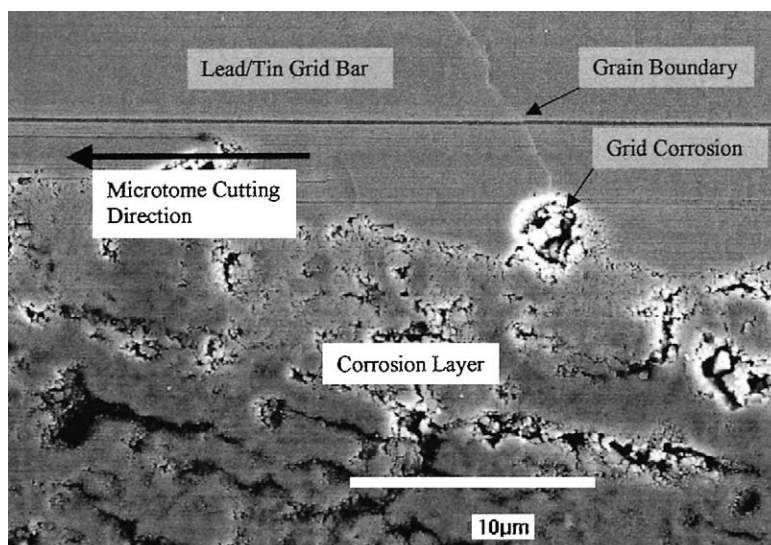Fig. 15. Grid corrosion layer interface from type E battery.

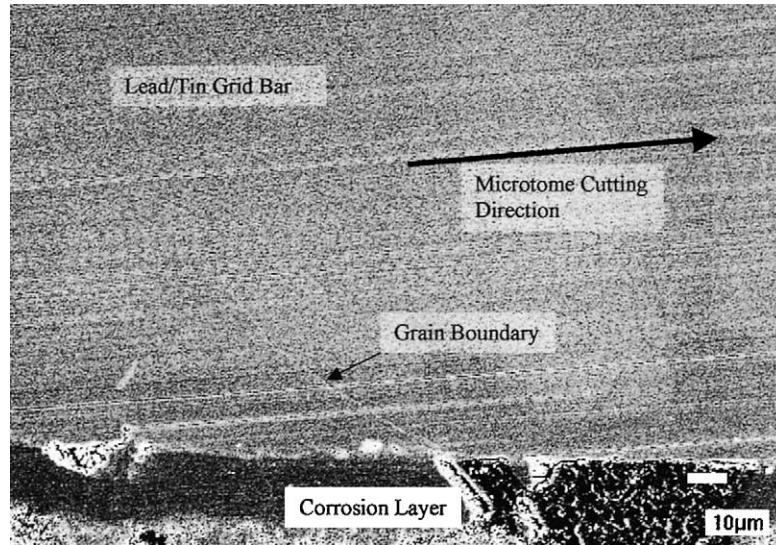Fig. 16. Corrosion propagating along grain boundary.

Fig. 17. Microtomed grid indicating position of grain boundary.

high definition pictures of both corrosion layer and interface morphology.

A significant feature observed in the photographs is the presence of 'fingers' of oxide growing into the lead/tin grids, but not into the pure lead. Corrosion layers produced from lead grids have a smooth grid/corrosion layer interface, however those growing from lead tin grids do not.

A more detailed examination of a lead/tin grid corrosion layer identified what was believed to be corrosion initiating in the region of a grain boundary, Fig. 16. Close examination of the grain boundary showed a small step to be present. A likely explanation is that the shearing action of the microtome's knife as it cuts a section from the alloy surface produces a force at the grain boundaries sufficient to cause a displacement, and the resulting step. The 'step'

was confirmed to be grain boundary by etching a section and comparing the location of the step with that of the grain boundary, revealed by the etched micrographs, Figs. 17 and 18.

Electron probe microanalysis was used to obtain values of the tin content within the grain and at the grain boundaries by taking numerous (17) randomly distributed analysis points at each position. The average percentage tin values obtained from the data for the grain and grain boundary regions were 0.75 and 0.96%, respectively. A statistical analysis using the Student's t-test indicated that there was a 0.2% or less probability of the two sample means obtained not being significantly different.

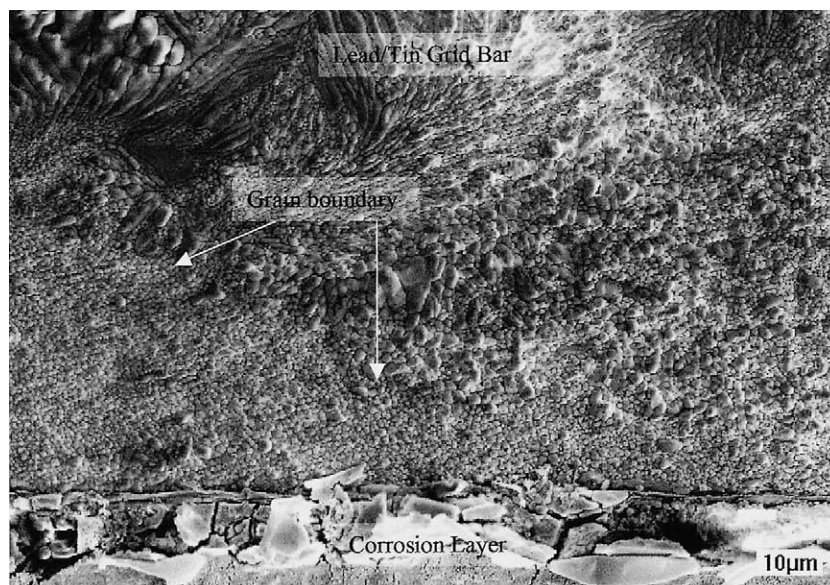The higher tin concentration observed at the grain boundary is due to the precipitation of tin in these regions during

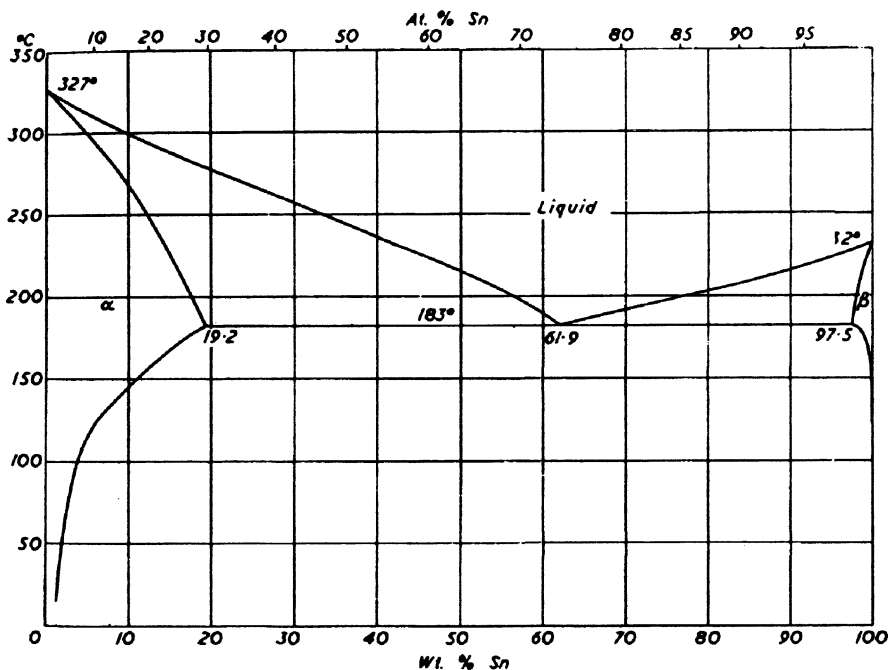Fig. 18. Etched grid indicating position of grain boundary.

Fig. 19. Lead/tin phase diagram (α = lead, β = tin).

solidification of the alloy. This can be expressed by the following phase reaction obtained from the appropriate position on the lead tin phase diagram shown in Fig. 19.

$$L \rightarrow L + \alpha \rightarrow \alpha \rightarrow \alpha + \beta \qquad (8)$$

As the molten alloy, L, cools during the casting procedure the α-phase, lead, solidifies. At very low temperatures, <50 °C the $\alpha + \beta$ region of the diagram is encountered and the β phase, tin, precipitates at the grain boundaries.

Corrosion is more likely to occur in the vicinity of the tin precipitates, as the higher concentration of tin will cause enhanced galvanic corrosion, due to the different electrode potentials of lead and tin. Thus, the electrochemical couple provides an ideal nucleus for the corrosion process.

7. Conclusions

The results indicate that corrosion layer thickness, structure and composition are influenced by PAM type and grid alloy. Corrosion layer thickness is related to the number of cycles. However, PAM and grid type appear to be the more influential factors.

Porosity in the corrosion layer was greater in electrodes with sulphated active materials. These layers were also significantly thicker than their non sulphated equivalent and it is believed that this is a result of an increased amount of oxygen reaching the grid/corrosion layer interface through the network of pores and cracks.

Optical and electron microscopy of corrosion layer cross-sections revealed bands identified by different colours/shades. However, the bands did not correspond to discrete

variations in oxide stoichiometry detected by electron probe microanalysis.

Battery types A and B, which achieved higher numbers of cycles to failure compared to types C–E, have on average a higher concentration of oxygen across the width of their corrosion layer. This indicates an increase in electronic conductivity and more efficient conduction across the corrosion layer.

Ultra-microtoming has been shown to be an effective method for preparation of grid/corrosion layer interfaces suitable for examination using electron optical techniques. Results showed that corrosion growth propagates along tin rich grain boundaries.

Acknowledgements

References

[1] D. Pavlov, A theory of the grid/positive active mass (PAM) interface and possible methods to improve PAM utilization and cycle life of lead/acid batteries, J. Power Sources 53 (1995) 9–21.
[2] D. Pavlov, The lead/acid battery lead dioxide active mass: a gel-crystal system with proton and electron conductivity, J. Electrochem. Soc. 139 (11) (1992) 3075–3080.

[3] G.J. May, Operational experience with valve regulated lead/acid batteries, J. Power Sources 53 (1995) 111–117.

[4] F. Lappe, Some physical properties of sputtered PbO_2 films, J. Phys. Chem. Solids 23 (1962) 1563–1572.

[5] A.F. Hollenkamp, K.K. Constanti, M.J. Koop, L. Apateanu, M. Calabek, K. Micka, Effects of grid alloy on the properties of positive-plate corrosion layers in lead/acid batteries. Implications for premature capacity loss under repetitive deep-discharge cycling service, J. Power Sources 48 (1994) 195–215.

[6] B. Monahov, D. Pavlov, Influence of antimony on the structure and the degree of hydration of the anodic PbO_2 layer formed an Pb–Sb electrodes, J. Electrochem. Soc. 141 (9) (1994) 2316–2326.

[7] D. Paolov, B. Monahov, Mechanism of action of Sn on the passivation phenomena in the lead/acid battery positive plate (Sn free effect), J. Electrochem. Soc. 136 (1989) 27–34.

[8] J. Garche, N. Anastasijevic, K. Wiesener, Electrochimica. Acta 26 (10) (1981) 1363–1373.

[9] R.F. Nelson, D.M. Wilson, J. Power Sources 33 (1991) 165–185.

[10] R.J. Ball, R. Evans, M. Deven, R. Stevens, Characterisation of defects observed within the positive grid corrosion layer of the valve regulated lead/acid battery, J. Power Sources 103 (2002) 207–212.

[11] Optimas 6.1, Optimas UK Ltd., West Maling, Kent, UK.